Statistical Distribution and Detection Limit of Time-Correlated Single-Photon Counting Echoes for Targets in Turbid Media

Quanchun Yu(余泉春), He Cai(蔡禾), Hongcheng Yin(殷红成),
and Liangsheng Li†(李粮生)

National Key Laboratory of Scattering and Radiation, Beijing, 100854, China

Strong scattering and absorption in turbid media severely limit the detection range and signal-to-noise ratio of conventional active optical detection methods. Leveraging the ultrahigh sensitivity and temporal resolution of single-photon detectors, this work establishes a statistical echo photon distribution model for targets in turbid media under the time-correlated single-photon counting (TCSPC) mode based on the diffusion equation, and proposes an object-to-background ratio (OBR) metric for quantitative performance evaluation. Experiments validate the model with a normalized cross-correlation coefficient above 0.97. Results show that effective detection and imaging ranges reach ~10 and ~5 times the scattering mean free path, respectively. Detection range increases logarithmically with laser repetition rate and single-pulse photon number, while noise and reflectivity show weaker influences. This study provides quantitative guidance for single-photon detection system design in turbid environments.

Keywords: Light diffuse, time-correlated single-photon detection, turbid media, diffusion equation.

PACS: 42.25.Bs, 42.25.Dd.

1. Introduction

Detection and imaging of targets in turbid media represent a critical challenge in medical imaging[1-8], autonomous driving[9-11], remote sensing[12], and underwater applications[13-17]. Turbid media significantly affect laser propagation through scattering and absorption effects: scattering induces beam broadening, energy attenuation, and polarization degradation; absorption causes photon energy loss. In the temporal domain, multiple scattering further prolongs optical path lengths and introduces path blur. Accurate calculation of light propagation in turbid media, and subsequent acquisition of light transmission characteristics, is a fundamental prerequisite for target detection, imaging, and recognition applications in such media.

Light propagation in turbid media is mainly simulated via Monte Carlo methods[18-21] or analytical methods[22-24]. The Monte Carlo method simulates light propagation by randomly sampling photon paths; it is applicable to complex turbid media environments and can accurately track scattering, absorption, and polarization changes, but entails high computational cost. Analytical methods (e.g., diffusion equation, radiative transfer equation) derive light intensity distributions based on physical models, offering high computational efficiency but limited applicability to complex turbid media such as anisotropic media.

† Corresponding author. E-mail: yuqc207@126.com

In recent years, single-photon detection devices such as single-photon avalanche diodes (SPADs) and superconducting nanowire single-photon detectors (SNSPDs) have developed rapidly, pushing optical signal detection sensitivity to the physical limit. They have been gradually applied in fields including underwater imaging, autonomous driving, and biological tissue imaging. Single-photon detection operates in two primary modes: photon counting mode and time-correlated single-photon counting mode. Photon counting mode achieves weak light detection by recording the number of incident photons per unit time, suitable for intensity measurements (e.g., fluorescence spectroscopy). The TCSPC mode extends dynamic range and temporal resolution through time tagging, enabling further analysis of photon arrival time distributions for ultrafast time-resolved applications such as fluorescence lifetime measurement and lidar.

Leveraging single-photon-level sensitivity and picosecond time resolution, time-correlated single photon counting (TCSPC) has become a core approach for characterizing the temporal transmission properties of photons in turbid media. Substantial studies have utilized TCSPC to observe pulse broadening and statistical distribution evolution of photons caused by multiple scattering in both atmospheric[25, 26] and aqueous[27, 28] turbid environments, and have developed scattering-adapted detection systems[29-31] and signal processing methods[32, 33] to steadily enhance the capture and analysis capacity of weak echo photons under high turbidity conditions.

Although single-photon detection technology and devices are increasingly mature, the transmission characteristics and statistical distribution of optical signals under the unique photon detection mode of single-photon detectors remain inadequately characterized. In this paper, based on the solution of the diffusion equation, we propose a statistical distribution model of echo photons from targets in turbid media under the TCSPC mode. We investigate the variation characteristics of echo photon statistical distributions under different detection system parameters and media turbidity levels. This study provides theoretical and experimental basis for evaluating the measurement capability of single-photon detection systems in turbid media and designing single-photon detection systems for specific turbid media.

2. Method

When pulsed laser is used for active detection of hidden objects inside scattering media, light undergoes the following propagation process: light incident along $+z$ direction into the scattering media diffuses to the target, is reflected by the target, and then diffuses back to the detector along $-z$ direction for detection. Assume a detector with a fixed reception direction $-z$, is placed at the light source position. The photon flux distribution at the detector can be expressed as:

$$J(\mathbf{r},t) = S(\mathbf{r},t) \otimes G(\mathbf{r},t) + n(\mathbf{r},t) \tag{1}$$

where $S(\mathbf{r},t)$ is the photon flux density distribution of the light source, $G(\mathbf{r},t)$ is the reflected photon flux density Green's function of the entire scattering media environment (including the scattering media itself and the hidden target within it), $n(\mathbf{r},t)$ is additive noise with a constant mean value and random distribution per unit time, and $\otimes$ denotes the 3D convolution operator acting on x,y,t.

Ignoring complex high-order interactions, $G(\mathbf{r},t)$ is considered as the sum of the photon flux density Green's function directly returned by the scattering media itself $G_{\mathrm{SM}}(\mathbf{r},t)$ and the photon flux density Green's function reflected by the hidden object $G_{\mathrm{Obj}}(\mathbf{r},t)$ [34-36], i.e.,

$$G(\mathbf{r},t) = G_{\mathrm{SM}}(\mathbf{r},t) + G_{\mathrm{Obj}}(\mathbf{r},t) \tag{2}$$

Assuming the pulse width of the light source is smaller than the system temporal resolution Δt, its distribution can be approximated as a delta function:

$$S(\mathbf{r},t) = N_0 \cdot \delta(\mathbf{r},t) \tag{3}$$

where N_0 is the number of photons contained in a single pulse.

The photon flux density at the detector receiving surface is $S(\mathbf{r},t) \otimes G(\mathbf{r},t)$. Let the minimum spatiotemporal voxel resolvable by the detection system be $\Delta V = \Delta x \Delta y \Delta t$, where $\Delta x, \Delta y, \Delta t$ are the minimum resolvable intervals of the detection system in the corresponding dimensions. The number of photons within a single spatiotemporal voxel is obtained by multiplying the photon flux density by the spatiotemporal voxel, and the expected detected photon number can then be calculated by further multiplying by the detector detection efficiency η. Furthermore, it is assumed that additive noise $n(\mathbf{r},t)$ exists in the detection process. The photon number distribution recorded by the detector is then:

$$\begin{aligned} J_{\mathrm{D}}(\mathbf{r},t) &= \eta \cdot \Delta V \cdot S(\mathbf{r},t) \otimes G(\mathbf{r},t) + n(\mathbf{r},t) \\ &= \eta \cdot \Delta V \cdot N_0 \cdot \left[G_{\mathrm{Obj}}(\mathbf{r},t) + G_{\mathrm{SM}}(\mathbf{r},t) \right] + n(\mathbf{r},t) \end{aligned} \tag{4}$$

Let N_{total} be the total number of photons contained in $J_{\mathrm{D}}(\mathbf{r},t)$. To avoid pile-up effects, we assume an attenuator is present such that the expected value of the total number of photons received by the detector per pulse return always equals 1. In practical experiments, a narrow time window aligned with the expected arrival time of the target echo can be adopted to suppress back-scattered light from the turbid medium, while a narrow bandpass filter can be utilized to reject ambient background light. If the photon count remains excessively high, the peak power of the laser can be appropriately reduced. Accordingly, the photon count distribution received by the detector is:

$$C\ \mathbf{r},t\ = f_{\text{rep}} \cdot t_{\text{acq}} \cdot \frac{J_{\text{D}}\ \mathbf{r},t}{N_{\text{total}}} \tag{5}$$

where f_{rep} is the laser repetition rate (which also equals the detector counting frequency assuming full detector response), t_{acq} is the accumulation time. The expressions for $G_{\text{Obj}}\ \mathbf{r},t$ and $G_{\text{SM}}\ \mathbf{r},t$ are given below.

2.1 Photon Flux Density Distribution Returned by the Scattering media

Assume a light source at position $\mathbf{r}_0 = \ 0,0,0$ emits a light pulse along direction $+z$ at time $t = 0$. Consider a semi-infinite scattering media occupying the space $z \geq 0$. The photon flux density distribution returned by the scattering media itself at a point $\mathbf{r} = \ x,y,0$ on the detection plane ($z = 0$ plane) — defined as the number of photons passing through unit area per unit time — can be calculated from the reflected photon flux density Green's function of the semi-infinite scattering media[22, 24]:

$$G_{\text{SM}}\ \mathbf{r},t\ = \frac{1}{2}\ 4\pi k\ ^{-\frac{3}{2}}\ t\ ^{-\frac{5}{2}} \mathrm{e}^{-\mu_{\text{a}} ct} \left\{ z_0 \mathrm{e}^{-\left(\frac{x^2+y^2+z_0^2}{4kt}\right)} +\ z_0 + 2z_{\text{e}}\ \ \mathrm{e}^{-\left[\frac{x^2+y^2+\ z_0+2z_{\text{e}}\ ^2}{4kt}\right]} \right\} \tag{6}$$

where $k = c/3\ \ \mu_{\text{a}} + \mu_{\text{s}}'$ is the diffusion coefficient, μ_{a} is the absorption coefficient, μ_{s}' is the reduced scattering coefficient, $z_0 = 1/\mu_{\text{s}}'$ is the scattering mean free path, t is time, c is the speed of light in the medium, and z_{e} is the extrapolated boundary distance.

2.2 Photon Flux Density Distribution Returned by the Hidden Object

Inside the scattering media, the light source generates a photon flux density $J^{+}\ \mathbf{r}',t'\ = G_{J-\text{h-inf}}^{\text{T}}\ \mathbf{r}' - \mathbf{r}_0,t'$ in direction $+z$ at target position $\mathbf{r}' = \ x',y',z$ at time t', where $G_{J-\text{h-inf}}^{\text{T}}$ is the transmitted photon flux density Green's function of the semi-infinite scattering media:

$$\begin{aligned} G_{J-\text{h-inf}}^{\text{T}}\ \mathbf{r},t\ = \frac{1}{2}\ 4\pi k\ ^{-\frac{3}{2}}\ t\ ^{-\frac{5}{2}} \mathrm{e}^{-\mu_{\text{a}} ct} \Bigg\{ & z - z_0\ \ \mathrm{e}^{-\left(\frac{x'^2+y'^2+\ z-z_0\ ^2}{4kt}\right)} - \\ & z + z_0 + 2z_{\text{e}}\ \ \mathrm{e}^{-\left[\frac{x'^2+y'^2+\ z+z_0+2z_{\text{e}}\ ^2}{4kt}\right]} \Bigg\} \end{aligned} \tag{7}$$

To simplify theoretical derivation, we simplify the interaction between light and the object as specular reflection [37]. For diffuse reflective targets, the reflected photon flux can be decomposed into components along the $-z$ direction (potentially

detectable) and the x and y directions (neglected in this model). For targets with complex three-dimensional morphologies, high-order reflections are neglected, and the target is discretized into multiple planar elements along the propagation direction for superposition calculation. After interaction with the object, photons generate a photon flux density $J^{-}\ \mathbf{r}',t''$ in direction $-z$ at time t''. Assuming the photon-object interaction is instantaneous, we have $t''=t'$. The reflected photon flux density $J^{-}\ \mathbf{r}',t''$ can be written as:

$$J^{-}\ \mathbf{r}',t''\ =G^{\mathrm{T}}_{J-\text{h-inf}}\ \mathbf{r}'-\mathbf{r}_0,t'\ R(\mathbf{r}')\delta\ t''-t' \tag{8}$$

where $R(\mathbf{r}')$ denotes the reflectivity of the object at position $\mathbf{r}'$. We assume an equivalent volumetric light source $q\ \mathbf{r}',t''$ is generated at position $\mathbf{r}'$, which is also the number of photons per unit volume per unit time.

$$q\ \mathbf{r}',t''\ =\frac{1}{\Delta z}\int G^{\mathrm{T}}_{J-\text{h-inf}}\ \mathbf{r}'-\mathbf{r}_0,t'\ R(\mathbf{r}')\delta\ t''-t'\ \mathrm{d}t' \tag{9}$$

where $\Delta z=v\cdot\Delta t$. The equivalent source $q\ \mathbf{r}',t''$ then continues to diffuse in the scattering media and eventually reaches the $z=0$ plane, producing a photon flux density $q\ \mathbf{r}',t''\ G^{\mathrm{T}}_{J-\mathrm{inf}}\ \mathbf{r}-\mathbf{r}',t-t''$ at position $\mathbf{r}=\ x,y,0$ on the $z=0$ plane at time t, where $G^{\mathrm{T}}_{\mathrm{J-inf}}$ is the transmitted photon flux density Green's function of the infinite scattering media:

$$G^{\mathrm{T}}_{\mathrm{J-inf}}\ \mathbf{r},t\ =\frac{1}{2}\ 4\pi k^{-\frac{3}{2}}t^{-\frac{5}{2}}z\mathrm{e}^{-\left(\mu_{\mathrm{a}}ct+\frac{x'^2+y'^2+z^2}{4kt}\right)} \tag{10}$$

Integrating over all positions and time yields the photon flux density distribution returned by the hidden object:

$$G_{\mathrm{Obj}}\ \mathbf{r},t\ =\iint q\ \mathbf{r}',t''\ G^{\mathrm{T}}_{J-\mathrm{inf}}\ \mathbf{r}-\mathbf{r}',t-t''\ \mathrm{d}t''\mathrm{d}\mathbf{r}' \tag{11}$$

Since the proposed method is derived from the diffusion equation, it maintains high accuracy only in the multiple-scattering regime. Generally, reliable results require a target depth greater than twice the scattering mean free path[38, 39]. In contrast, when the target depth is less than one scattering mean free path, insufficient scattering events introduce substantial errors, making the diffusion model inapplicable.

3. Experimental results

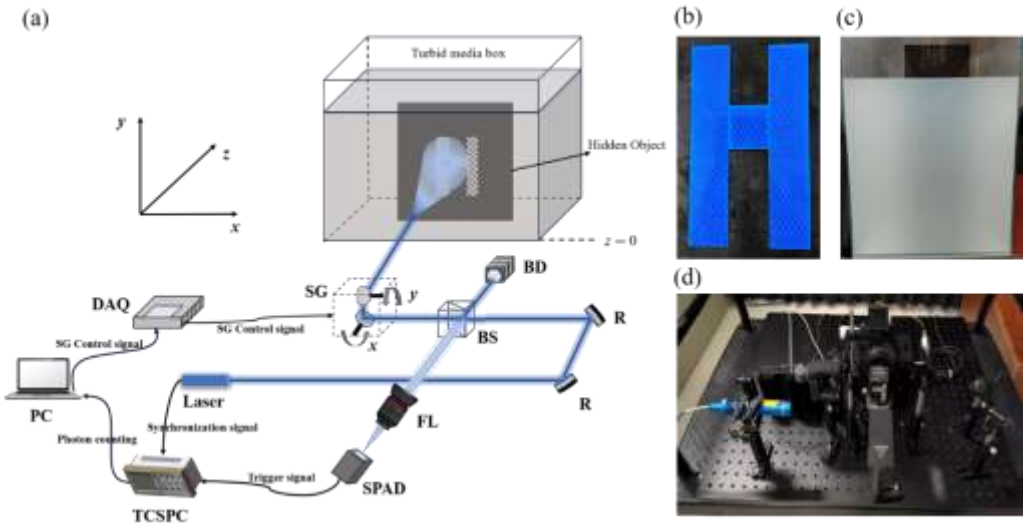


Fig. 1 (a) Schematic diagram of the confocal single-photon detection setup; (b) Photograph of the hidden object; (c) photograph of the object immersed in turbid water; (d) photograph of the optical section of the confocal single-photon detection setup. DAQ: data acquisition card; SG: scanning galvanometer; BS: beam splitter; BD: beam dump; R: reflector; FL: focusing lens; SPAD: single-photon avalanche diode; TCSPC: time-correlated single-photon counting module.

We conducted imaging experiments using the confocal single-photon experimental setup shown in Fig. 1. The laser emits a series of picosecond pulses that propagate to the beam splitter (BS). A portion of the light is reflected to the beam dump (BD) and absorbed, while the remaining portion transmits through the BS and continues to the scanning galvanometer (SG). A personal computer (PC) controls the data acquisition card (DAQ) to output electrical signals for SG steering, enabling the SG to reflect the pulsed laser onto 32×32 grid points on the surface of the turbid media tank, covering a scanning area of 20 cm × 20 cm.

The reflection optical path shares a portion of the incident optical path. Reflected light returns along the original path to the BS; part of the transmitted light is discarded, while the reflected light propagates to the focusing lens (FL) and is focused onto the photosensitive chip of the SPAD for detection. Simultaneously with each pulse emission, the laser outputs a synchronization electrical signal to the SPAD, which activates the gating window to prepare for photon reception. The synchronization signal is also fed to the TCSPC module as the start time for each photon counting cycle. When a photon is detected, the SPAD outputs a trigger electrical pulse to the TCSPC as the photon arrival signal. The time-of-flight (ToF) of an individual photon is obtained by subtracting the start time from the arrival time.

While the SG directs the beam to a single grid point on the turbid media tank, the laser emits pulses continuously at a fixed frequency. The TCSPC accumulates the ToF of a large number of photons, yielding a set of photon count statistics across different flight times, which are then transmitted to the PC for storage. Through the above experimental procedure, a set of three-dimensional (x, y, t) photon statistical data is

ultimately obtained.

The laser used in the experiment is the PICOPOWER-LD-450-FSB manufactured by ALPHALAS, which generates pulsed light at a wavelength of 450 nm with a maximum repetition rate of 50 MHz, a maximum average power of 5 mW, and a pulse duration of 50 ps. The TCSPC module is the PicoHarp 300 from PicoQuant, with a maximum photon counting rate of 10 MHz. The SPAD is the PD-050-CTE from Micro Photon Devices, with a dead time of 73.7 ns, dark count rate of 12.2 counts/s, and maximum trigger rate of 13.5 Mc/s. The SG is the GVS212 from THORLABS, featuring biaxial rotation with a maximum rotation angle of 40°. The DAQ is the USB-6343 from National Instruments, and the FL is the AF-S Nikkor 50 mm f/1.4G from Nikon.

In the experiment, the laser was configured with a repetition rate of 4 MHz, an average power of 0.18 mW, a peak power of 750 mW, and a single-pulse energy of 37.5 pJ. A glass tank with dimensions of 40 cm × 40 cm × 40 cm (length × width × height) was used as the turbid media container. The tank was filled with water, and 300 mL of milk-containing beverage was added and stirred uniformly to serve as the turbid media. The optical parameters were calibrated using the time-resolved reflection method[22]. First, the temporal distribution of back-scattered photons from the pure turbid medium without hidden targets was measured. The Levenberg–Marquardt fitting was then performed on the measured temporal waveform using the analytical solution of the diffusion equation for a semi-infinite media. The fitted optical parameters of the experimental medium are $\mu_s' = 12.62\text{m}^{-1}$ and $\mu_a = 0.08\text{m}^{-1}$, corresponding to a reduced scattering mean free path z_0 of 7.94cm. A blue reflective sticker cut into the letter “H” and attached to a black frosted acrylic plate was used as the target, with a reflectivity of 0.32. The target was placed at depths of 16 cm, 17.5 cm, and 19 cm, respectively. The measured and theoretically calculated target photon count distributions are shown in Fig. 2.

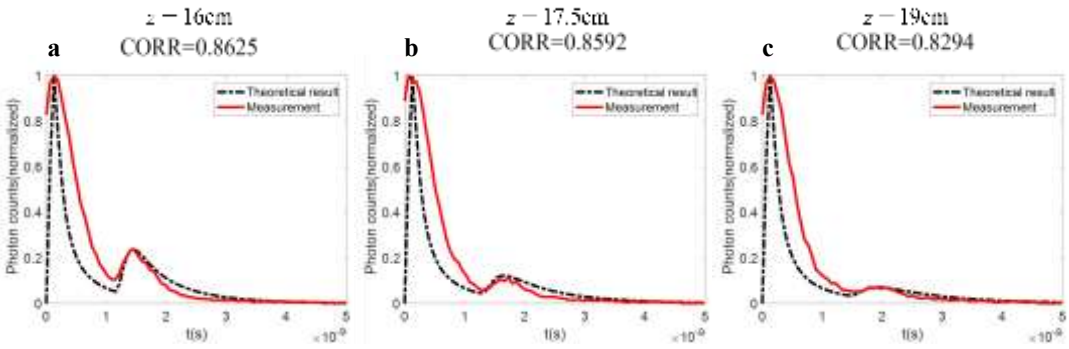


Fig. 2 Photon counting distributions with hidden target placed at (a)z=16 cm, (b)z=17.5 cm, and (c)z=19 cm.

In the three subplots of Fig. 2, the first and tallest peak corresponds to photons backscattered by the scattering media itself, while the second shorter peak

corresponds to photons returned from the target. For ease of comparison, photon counts are normalized to the peak value of the first peak. When the target was placed at depths of 16 cm, 17.5 cm, and 19 cm, the normalized cross-correlation coefficients (CORR) between the measured and theoretically calculated results were 0.8625, 0.8592, and 0.8294, respectively.

Since the diffusion equation exhibits larger errors near the light source, we only intercepted photons returned from the target for comparison — a procedure practically implementable via time gating. Under this condition, the normalized cross-correlation coefficients (CORR) between measurement and theory were 0.9734, 0.9739, and 0.9702 for target depths of 16 cm, 17.5 cm, and 19 cm, respectively.

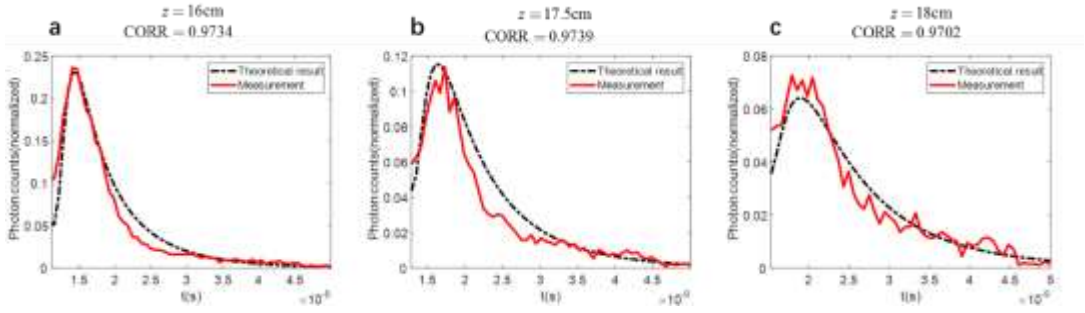


Fig. 3 Photon counting distributions only retaining photons reflected from the hidden target at (a)16 cm, (b)17.5 cm, and (c)19 cm.

4. Results and Discussion

We set $\mu_s' = 1\mathrm{m}^{-1}$, $\mu_a = 0.02\mathrm{m}^{-1}$ and adopted a flat target with reflectivity of 1 and an area of $1\mathrm{m}^2$ placed on the $z = 3\mathrm{m}$ plane. The laser had a single-pulse photon number $N_0 = 1\times10^9$, a repetition rate $f_{\mathrm{rep}} = 10\mathrm{MHz}$, and an accumulation time $t_{\mathrm{acq}} = 1\mathrm{s}$. Both the incident and detection positions were at the origin $0,0,0$. The average number of noise photons N_{noise} within a 64 ps time interval was 5. Based on the theoretical method presented in Section 2, the distribution of $C\ r,t$ is shown in Fig. 4.

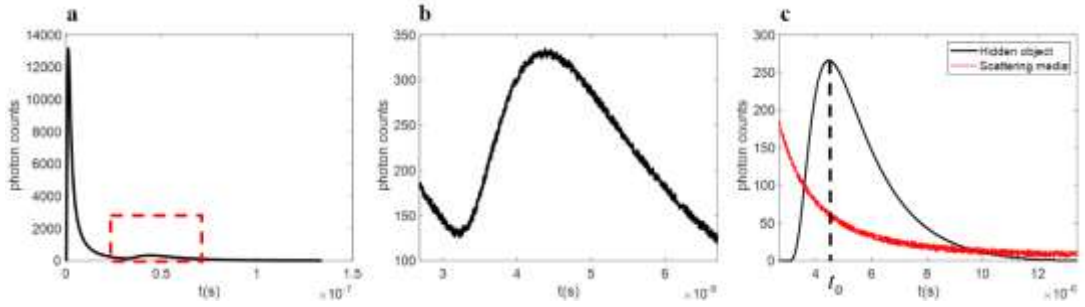


Fig. 4 Photon count distribution received by the SPAD. (a) Total photon count distribution, with the hidden object peak marked by the red dashed box; (b) magnified view of the photon count distribution in the hidden object region; (c) comparison between the photon count distribution returned by the hidden object and the background photon distribution.

To quantitatively evaluate the effectiveness of detection and imaging, we define the object-to-background ratio (OBR) as the ratio of the photon count returned by the hidden object to the background photon count at the target peak time t_0:

$$OBR = \frac{N_0 \cdot \Delta V \cdot G_{\mathrm{Obj}}\ r, t_0}{N_0 \cdot \Delta V \cdot G_{\mathrm{SM}}\ r, t_0\ + t_{\mathrm{acq}} \cdot n\ r, t_0} \tag{12}$$

We consider that a target can be effectively detected when $\mathrm{OBR} \geq 1$, indicates that the number of photons reflected from the target exceeds that of the background photons, while effective imaging of the target requires the photon counts backscattered from the target to be several times higher than background photon counts to maintain a sufficient signal-to-noise ratio. In our previous work, we verified that this threshold multiple is approximately 3, i.e., $\mathrm{OBR} \geq 3$ [37].

In general, the photon reception time window of the detector should be set appropriately. An excessively short time window may result in incomplete photon distribution reception, while an excessively long-time window increases the probability of detecting noise photons. Under a limited number of detection events, this further reduces the probability of detecting the hidden object signal. An effective approach is to implement time gating on the detector, which opens only at the expected arrival time of photons from the hidden object. This method suppresses irrelevant noise in the temporal domain, thereby allocating more detection events to photons returned from the hidden object of interest. We demonstrate in Fig. 5 that time gating can effectively improve OBR under the same detection system.

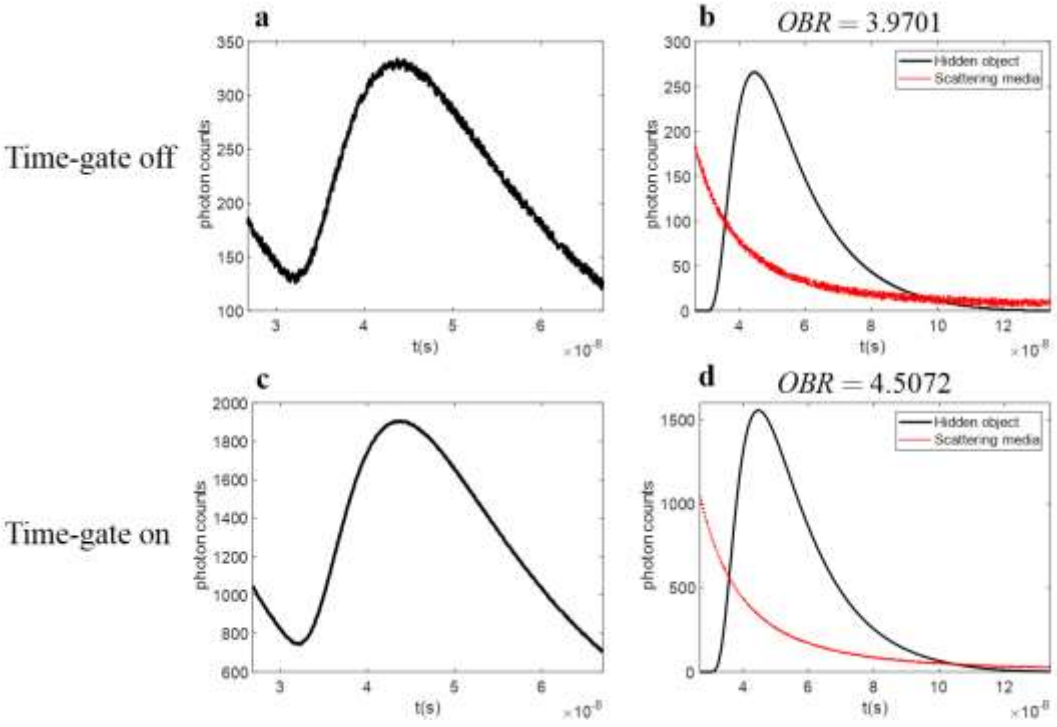


Fig. 5 Photon count distributions returned by the hidden object with and without time gating. (a–b)

Photon count distribution and comparison between hidden object and background distributions with time gating enabled; (c–d) photon count distribution and comparison with time gating disabled.

With all detection system parameters unchanged, the OBR was 3.9701 when time gating was disabled. When time gating was activated at $t = 2.6816 \times 10^{-8}\,\mathrm{s}$ (as shown in Fig. 5(c)), the OBR increased to 4.5072, corresponding to a 13.5% improvement.

We further investigated the relationship between OBR and hidden object depth. The μ_s' was set from 10 to $100\,\mathrm{m}^{-1}$, and the distribution of OBR as a function of hidden object position is shown in Fig. 6. The two red horizontal lines represent the thresholds for effective detection and effective imaging of the hidden object, respectively. As depth *z* increases, OBR decreases rapidly.

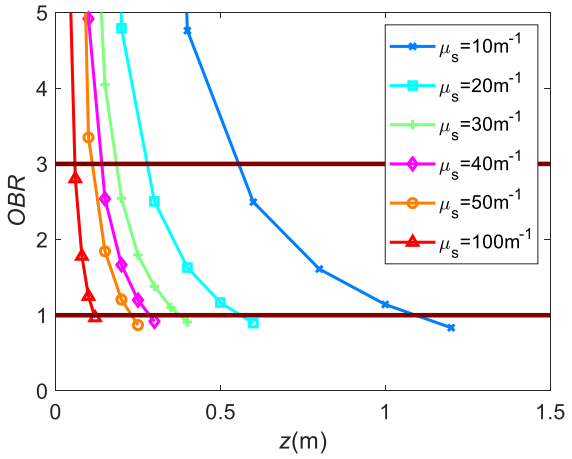


Fig. 6 OBR distribution as a function of hidden object depth.

We further calculated the maximum ranges for effective detection and effective imaging of the hidden object, and examined their relationship with μ_s', as shown in Fig. 7.

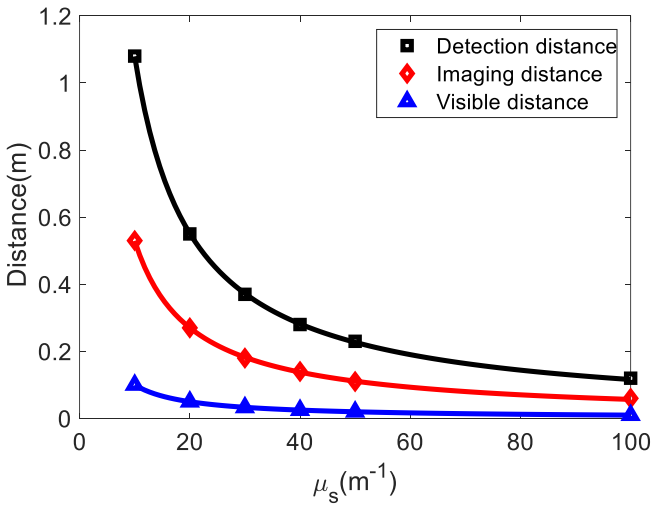


Fig. 7 Distributions of maximum effective detection range, maximum effective imaging range, and

visibility range as functions of μ_s'

In Fig. 7, red data points represent the maximum imaging distance d_I, black data points represent the maximum detection distance d_D, and the blue line denotes one scattering mean free path in the turbid media, representing the visibility distance in the turbid media. We fitted the distributions of d_I and d_D versus μ_s' and found that both follow a power-law distribution, as shown by the red and black curves in Fig. 7:

$$\begin{aligned} d_I &= a_I \cdot \mu_s'^{b_I} \\ d_D &= a_D \cdot \mu_s'^{b_D} \end{aligned} \tag{13}$$

where $a_I = 4.938, b_I = -0.9697, a_D = 10.04, b_D = -0.9686$. The goodness-of-fit R^2 values for d_I and d_D are 0.9998 and 0.9999, respectively, indicating excellent agreement between the fitting results and the data points.

In the equation (13), both b_I and b_D are close to −1, while $\mu_s'^{-1}$ is the scattering mean free path — the average distance a photon travels between two successive scattering events in the medium. Therefore, the equations indicate that the effective detection and imaging ranges for hidden objects are approximately 10 times and 5 times the scattering mean free path, respectively. In Fig. 7, the imaging range is on average approximately 5.54 times the visibility range.

We further analyzed the effects of laser pulse repetition rate f_{rep}, single-pulse photon number N_0, and average noise photon number N_{noise} on the detection distance, with results shown in Fig. 8. Open-ocean seawater was used as the scattering media, with a reduced scattering coefficient of $\mu_s' = 0.037\text{m}^{-1}$ and an absorption coefficient of $\mu_a = 0.114\text{m}^{-1}$. The default detection system parameters were: $N_{\text{emit}} = 1\times10^9$, $f_{\text{rep}} = 1\times10^6\,\text{Hz}$, accumulation time $t_{\text{acq}} = 1\text{s}$, with both incident and detection positions at the origin $0,0,0$. The average number of noise photons N_{noise} within a 64 ps time interval was 5.

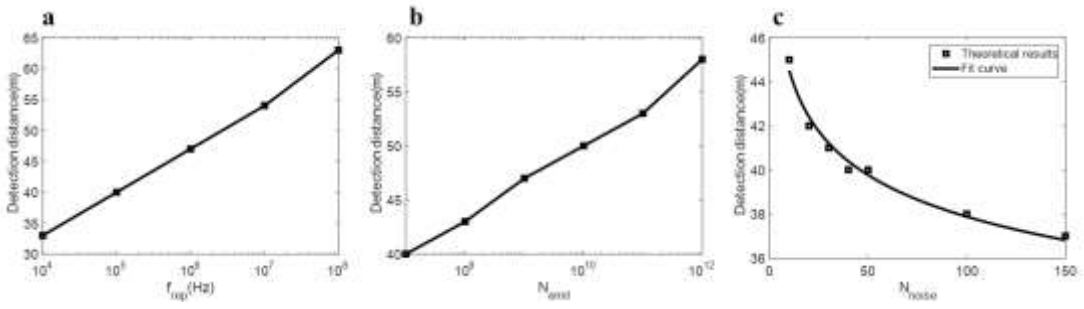


Fig. 8Variation of detection distance with (a) f_{rep}, (b) N_0, and (c) N_{noise}.

As can be seen from Fig. 8, the detection distance increases logarithmically with f_{rep} and N_0, while it decreases in a power-law manner with increasing N_{noise}. The expression of the fitted curve in Fig. 8(c) is $d_D = 52.32 \cdot N_{\text{noise}}{}^{-0.07015}$.

5. Conclusion

In this work, we establish an analytical statistical model for echo photon distributions of hidden targets in turbid media under the time-correlated single-photon counting (TCSPC) regime, derived from the diffusion approximation of radiative transfer. To quantify detection performance, we introduce the object-to-background ratio (OBR) as a metric to define the effective detection range and effective imaging range. The model is validated via confocal single-photon experiments, yielding a normalized cross-correlation coefficient above 0.97 for target echo signals.

Calculation results reveal that both the maximum effective detection range and imaging range follow a power-law relationship with the reduced scattering coefficient of the turbid media. Specifically, the effective detection range reaches approximately 10 times the scattering mean free path, while the effective imaging range reaches approximately 5 times the scattering mean free path, markedly exceeding the conventional visibility limit in turbid media. We further systematically characterize the influence of system parameters on detection performance. The results show that the detection range increases logarithmically with laser pulse repetition rate and single-pulse photon number, whereas the average noise photon count and target reflectivity exert relatively weaker effects. Time gating is confirmed as an effective approach to enhance OBR, delivering a 13.5% improvement under the tested configuration.

This study provides a quantitative theoretical framework for understanding photon transport and single-photon detection characteristics in turbid media. The derived scaling laws and parameter sensitivity conclusions can serve as practical guidelines for the design and optimization of long-range single-photon detection systems applied to underwater exploration, atmospheric remote sensing, and biomedical imaging.

Data availability statement
The datasets generated and/or analyzed during the current study are available from the corresponding author on reasonable request.

Acknowledgment
This work is supported by Ministry of Science and Technology of China, 210222.

References

[1] Ntziachristos V 2010 Nature Methods 7 603-614

[2] Yoon S, Kim M, Jang M, Choi Y, Choi W, Kang S, and Choi W 2020 Nature Reviews Physics 2 141-158
[3] Eggebrecht A T, Ferradal S L, Robichaux-Viehoever A, Hassanpour M S, Dehghani H, Snyder A Z, Hershey T, and Culver J P 2014 Nature Photonics 8 448-454
[4] Bertolotti J, and Katz O 2022 Nature Physics 18 1008-1017
[5] Shikhaliev P M 2015 Physics in Medicine & Biology 60 2453 - 2474
[6] Li Q, Zeng J, Miao Q, and Gao M 2019 Frontiers in Bioengineering and Biotechnology 7
[7] Ruan H, Liu Y, Xu J, Huang Y, and Yang C 2020 Nature Photonics 14 511 - 516
[8] Michalska J M, Lyudchik J, Velicky P, Štefaničková H, Watson J F, Cenameri A, Sommer C, Amberg N, Venturino A, Roessler K, Czech T, Höftberger R, Siegert S, Novarino G, Jonas P, and Danzl J G 2024 Nature Biotechnology 42 1051-1064
[9] Zhang Y, Li S, Sun J, Zhang X, Liu D, Zhou X, Li H, and Hou Y 2022 Optics express 30 34497-34509
[10] Xiao J, Shen M, Lei J, Zhou J, Klette R, and Sui H 2020 Neurocomputing 389 108-122
[11] Xu G, Wang X, and Xu X 2020 IEEE/CAA Journal of Automatica Sinica 7 1649-1661
[12] Li D, Lin B, Wang X, and Guo Z 2022 IEEE Transactions on Geoscience and Remote Sensing 60 1-10
[13] Maccarone A, Mattioli Della Rocca F, McCarthy A, Henderson R, and Buller G S 2019 Opt Express 27 28437-28456
[14] Zhao F, Lu R-T, Chen X, Jin C, Chen S, Shen Z, Zhang C, and Yang Y 2021 Laser & Photonics Reviews 15
[15] Yang X, Yu Z, Xu L, Hu J, Wu L, Yang C, Zhang W, Zhang J, and Zhang Y 2021 Opt. Express 29 18 28388-28405
[16] Joshi R, Usmani K, Krishnan G, Blackmon F, and Javidi B 2024 Optics express 32 1789-1801
[17] Zhao Y, He W, Ren H, Li Y, and Fu Y 2022 Optics and Lasers in Engineering 148 106777
[18] Jönsson J, and Berrocal E 2020 Optics express 28 37612-37638
[19] Ramella-Roman J C, Prahl S A, and Jacques S L 2005 Optics express 13 4420-4438
[20] Liao Y, Shangguan M, Yang Z, Lin Z, Wang Y, and Li S 2023 Remote Sensing 15 5245
[21] Huang Y, He Y, Zhu X, Xu G, and Zhang C 2025 Optics Communications 574 131157
[22] Patterson M S, Chance B, and Wilson B C 1989 Applied optics 28 2331-2336
[23] Chandrasekhar S 1943 Reviews of Modern Physics 15 1-89
[24] Contini D, Martelli F, and Zaccanti G 1997 Applied optics 36 19 4587-4599
[25] Qiao K, Yang J, and Jin C 2022 Infrared and Laser Engineering 51 20220404-20220401-20220404-20220413
[26] Tobin R, Halimi A, McCarthy A, Soan P J, and Buller G S 2021 Scientific Reports 11 11236
[27] Maccarone A, McCarthy A, Ren X, Warburton R E, Wallace A M, Moffat J, Petillot Y, and Buller G S 2015 Optics express 23 33911-33926
[28] Halimi A, Maccarone A, Lamb R A, Buller G S, and McLaughlin S 2021 IEEE Transactions on Computational Imaging 7 961-974
[29] Maccarone A, Acconcia G, Steinlehner U, Labanca I, Newborough D, Rech I, and Buller G S 2021 Sensors 21 4850
[30] Zhang R, Martin G M, Henderson R K, Buller G S, Gyongy I, and Maccarone A 2026 Optics express 34 5366-5381
[31] Shangguan M, Li Y, Mo Y, Wang J, and Huang T 2025 Optics letters 50 1957-1960
[32] Song K, Liu H, Bian Y, Wang D, Hu J, Zhao S, Zhao Z, and Xiao L 2026 14 1588
[33] Zeng F, Bian Y, Song K, Liu H, Zhao S, Wang X, Zhang F, Ge H, Wang D, and Xiao L 2025 APL Photonics 10
[34] Arridge S R 1999 Inverse Problems 15 R41
[35] Arridge S R, and Schotland J C 2009 Inverse Problems 25 123010
[36] Gibson A P, Hebden J C, and Arridge S R 2005 Physics in Medicine & Biology 50 R1
[37] Yu Q, Cai H, Zhu X, Yin H, and Li L 2025 Optics and Lasers in Engineering 194 109126
[38] Farrell T J, Patterson M S, and Wilson B 1992 Medical Physics 19 879-888

[39] Kienle A, and Patterson M S 1997 J. Opt. Soc. Am. A 14 246-254